Scilight

eChem
https://www.sciltp.com/journals/eChem

Article

Spin State Modulation of MnO_2 by Zn-Doping for Enhanced Supercapacitor and Hydrogen Evolution

Juyin Liu [1], Xue Zhang [2], Xuefeng Wu [1], Jingping Hai [1], Xiyuan Li [1], Ruming Feng [1],* and Yanfang Gao [2],*

[1] Inner Mongolia Daqingshan Laboratory, Hohhot 017000, China
[2] School of Chemical Engineering, Inner Mongolia University of Technology, Hohhot 010051, China
* Correspondence: 459159374@qq.com (R.F.); yf_gao@imut.edu.cn (Y.G.)

How To Cite: Liu, J.; Zhang, X.; Wu, X.; et al. Spin State Modulation of MnO_2 by Zn-Doping for Enhanced Supercapacitor and Hydrogen Evolution. *eChem* **2026**, *2*(1), 5. https://doi.org/10.53941/echem.2026.100005

Received: 28 March 2026
Revised: 25 May 2026
Accepted: 26 May 2026
Published: 24 June 2026

Abstract: Manganese dioxide (MnO_2) stands out as a promising multifunctional material for supercapacitors and hydrogen evolution reaction (HER) owing to its high theoretical capacitance, rich valence states, low cost, and environmental friendliness. However, the strong Jahn-Teller effect induces electron localization in Mn^{3+}, giving rise to poor intrinsic conductivity, sluggish charge transport, and structural instability, which severely restricts its practical applications. Herein, a series of Zn-doped MnO_2 was synthesized through a facile hydrothermal method to modulate the spin state and electronic structure of MnO_2. Zn doping triggered local lattice distortion, broke the symmetric octahedral field of [MnO_6], and optimized the occupation of Mn 3d orbitals, thereby enhancing spin polarization and promoting d-electron delocalization. Systematic characterizations and density functional theory (DFT) calculations verified that Zn doping reduced the bandgap of MnO_2 from 1.7 eV to 1.1 eV, increased the e_g orbital occupancy, and generated abundant oxygen vacancies and electrochemically active sites, which significantly improved electron mobility and ion diffusion kinetics. As the supercapacitor cathode, the assembled Zn-MnO_2//La-MoO_3/GQDs asymmetric supercapacitor achieved a maximum energy density of 23.9 Wh kg^{-1} with 80.9% capacitance retention after 6000 cycles. Meanwhile, as an electrocatalyst for HER in 1 M KOH, 1% Zn-MnO_2 exhibited a lower overpotential of 161 mV at 10 mA cm^{-2} and a small Tafel slope of 85 mV dec^{-1}, with outstanding stability after 5000 cycles. This work demonstrated that Zn doping-induced spin state modulation effectively addressed the inherent limitations of MnO_2, providing a feasible strategy for designing high-performance Mn-based materials for integrated energy storage and conversion applications.

Keywords: manganese dioxide; spin state; supercapacitor; hydrogen evolution reaction

1. Introduction

With the continuous growth of global energy demand and the increasingly severe environmental problems caused by fossil fuel consumption, the development of efficient and sustainable energy storage and conversion technologies has become an urgent scientific and technological priority. Among various emerging systems, supercapacitors and electrocatalytic hydrogen evolution reaction (HER) technologies have attracted extensive attention owing to their important roles in clean energy utilization [1]. Supercapacitors are considered promising energy-storage devices because of their high- power density, rapid charge/discharge capability, and long cycling life, while HER is recognized as a key half-reaction for green hydrogen production and an essential process for

Copyright: © 2026 by the authors. This is an open access article under the terms and conditions of the Creative Commons Attribution (CC BY) license (https://creativecommons.org/licenses/by/4.0/).
Publisher's Note: Scilight stays neutral with regard to jurisdictional claims in published maps and institutional affiliations.

constructing a carbon-neutral energy system [2]. Nevertheless, the practical applications of these two technologies are still restricted by the low energy density of electrode materials in supercapacitors and the high cost, as well as the insufficient durability of efficient HER catalysts.

Transition metal oxides are promising multifunctional materials for electrochemical energy storage and catalysis due to their rich redox chemistry, abundance, low cost, and environmental compatibility. Among them, manganese dioxide (MnO_2) is particularly attractive for supercapacitors and HER applications [3,4], because of its high theoretical capacitance, diverse structures, low toxicity, and the favorable electrochemical activity endowed by the unsaturated coordination environment and variable valence states of Mn [5,6]. However, its poor electrical conductivity limits practical performance, leading to lower actual capacitance and sluggish reaction kinetics [7]. Thus, researchers have developed modification strategies including introducing oxygen vacancies to enhance intrinsic conductivity [8], constructing manganese vacancies to shorten ion diffusion paths [9], and optimizing charge transfer through heterogeneous interfaces [10]. Despite some progress, overcoming the limitations imposed by the electronic structure of MnO_2 remains a major challenge. The primary reason for the difficulty is the Jahn-Teller effect, which causes electron localization in Mn^{3+}, thereby restricting electron transport and leading to structural instability. Most studies attribute electrochemical changes to lattice distortions caused by transition metal ion doping [11,12]. These lattice distortions are often accompanied by d-orbital restructuring. Although they have demonstrated widespread application potential in the field of electrocatalysis, related research in the energy storage is still insufficient.

Recently, spin-state engineering has served as an emerging strategy for regulating electronic structure, offering a new perspective for overcoming the limitations of traditional modification methods [13–15]. By modulating the spin configuration of transition metal ions, spin-state regulation can directly influence orbital occupancy, electron distribution, metal-oxygen covalency, and the adsorption/desorption behavior of reaction intermediates, thereby optimizing intrinsic activity and electrochemical kinetics [16–19]. The approach proves particularly significant for MnO_2 systems. As previously mentioned, the electronic localization caused by the Jahn-Teller distortion of Mn^{3+} forms the root of performance degradation [20]. Regulating the spin states can alleviate this localization effect to promote electron transitions while simultaneously releasing accumulated lattice stress, providing a pathway to synergistically address the dual challenges of poor conductivity and structural instability. Cation doping is one of the most effective methods for regulating the spin states of transition metal oxides [14,21]. Here, Zn^{2+} stands out due to its abundant global reserves, low cost, and unique closed-shell electron configuration ($3d^{10}4s^2$), which enables a doping mechanism distinct from that of traditional variable-valent metal ions [22]. Different from doping methods that introduce additional redox pairs, Zn^{2+} exerts its effect by inducing local lattice distortion to form cationic defects and generating electron coupling effects [23]. This characteristic makes the regulation process more controllable and effectively avoids by-products arising from the introduction of complex valence state changes. Previous studies have clearly demonstrated that the introduction of Zn^{2+} into the MnO_2 lattice effectively induces the formation of oxygen vacancies and structural defects, which not only create more electrochemically active sites but also significantly improve the kinetic conditions for electron transport and ion diffusion [24,25]. Furthermore, studies in other transition metal systems have shown that the addition of Zn^{2+} can lead to localized symmetry breaking, accompanied by [CoO_6] octahedral distortion and Co 3d orbital restructuring or changes in electronic structure and bonding characteristics through slight lattice distortion [26,27]. Hence, the combined enhancement of energy storage capacity and hydrogen evolution catalytic activity in MnO_2 can be achieved by regulating the electronic configuration of the Mn centers through the incorporation of Zn^{2+} into the MnO_2 lattice.

In this work, a series of Zn-doped MnO_2 materials was synthesized through a simple hydrothermal method to systematically investigate the effects of zinc doping on the crystal structure, lattice distortion, spin state distribution, and electrochemical behavior of MnO_2. Through structural characterization, electrochemical measurements, and density functional theory (DFT) calculations, the effects of Zn^{2+} introduction on charge transfer, spin polarization of Mn 3d orbitals, and reaction kinetics were clarified. Moreover, the optimized Zn-MnO_2 was used as the cathode for an asymmetric supercapacitor and as a hydrogen evolution catalyst, further demonstrating its practical potential as a multifunctional electrochemical material. This work provides new insights into the regulation of spin states through non-redox cation doping and offers a viable strategy for the rational design of manganese-based materials for integrated energy storage and energy conversion applications.

2. Experimental

2.1. Preparation of δ-MnO$_2$

0.19 g $KMnO_4$ and 0.034 g $MnSO_4 \cdot H_2O$ were placed in a beaker, and 40 mL of deionized water was added with continuous stirring for 30 min to obtain a well-mixed solution. The mixture was transferred to a 100 mL tetrafluoroethylene hydrothermal reactor and heated at 160 °C for 16 h. After being cooled to room temperature, the mixture was washed six times by centrifugation with alternating deionized water and anhydrous ethanol for 5 min each. The product δ-MnO_2 was then vacuum-dried at 60 °C for 10 h.

2.2. Preparation for Zn-MnO$_2$

0.19 g $KMnO_4$ and 0.034 g $MnSO_4 \cdot H_2O$ were placed in a beaker, and 40 mL of deionized water was added with continuous stirring for 30 min to obtain a well-mixed solution. 4 mg, 12.1 mg, and 20.1 mg of $ZnSO_4 \cdot 7H_2O$ were added to the mixed solution, respectively, and continued to stir for 30 min. The mixed solution was transferred to a hydrothermal reactor and heated at 160 °C for 16 h. After being cooled to room temperature, the mixture was washed six times by centrifugation with alternating deionized water and anhydrous ethanol for 5 min each. The samples were vacuum dried at 60 °C for 10 h to obtain the product C-Zn-MnO_2, which were labeled 1%Zn-MnO_2, 3%Zn-MnO_2, and 5%Zn-MnO_2, respectively.

2.3. Characterization Methods

Materials, characterization, electrochemical measurements, and electrochemical tests can be found in the Supporting Information.

2.4. Theoretical calculations

All calculations were performed within the framework of density functional theory (DFT) using the projector augmented plane-wave (PAW) method, as implemented in the Vienna ab initio simulation package (VASP) [28]. In the theoretical calculations of band structures and density of states, the generalized gradient approximation (GGA) proposed by Perdew, Burke, and Ernzerhof was selected for the exchange-correlation potential, with the cut-off energy for plane waves set to 500 eV [29]. The energy criterion for the iterative solution of the Kohn-Sham equation was set to 10^{-5} eV, and a 3 × 3 × 1 k-mesh was adopted for the Brillouin zone integration. To accurately handle the strong correlation effect of Mn 3d electrons, a modified DFT + U method was employed in this study, where a Hubbard correction of $U = 3.42$ eV was applied to Mn atoms, and the Coulomb attraction between the inner and outer electrons of each atomic nucleus in the system was treated as an ultra-pseudopotential. All structures were geometrically optimized until the residual forces on the atoms were reduced to less than 0.02 eV/Å.

3. Results and Discussion

The morphological transformation of MnO_2 samples with different Zn doping concentrations (0%, 1%, 3%, and 5%) was analyzed using Scanning Electron Microscope (SEM). As shown in Figure S1a, δ-MnO_2 formed a layered nanoflower structure with a smooth surface and a densely stacked arrangement through the curved self-assembly of nanosheets. The nanosheet framework was maintained with a Zn doping concentration of 1%, but interlayer folds increased and the stacked density rose significantly (Figure S1b). This indicated that the introduction of low-concentration Zn may promote directed attraction between adjacent nanosheets through electrostatic interactions, thereby enhancing the compactness of interlayer assembly and suppressing disordered dispersion of the nanosheets. When the Zn doping concentration was further increased to 3%, the interlayer stacking density of the nanosheets decreased, and partial regions exhibited slight curling of the nanosheet edges, though the complete nanoflower structure was still maintained (Figure S1c). This behavior may result from Zn^{2+} concentration gradients distributed between layers, which trigger internal stress rearrangement within the crystal, partially neutralize surface electrical charges on the nanosheets, and weaken interlayer electrostatic attractions. This process was coupled with preferred adsorption at high-energy edge sites, inducing changes in the curvature of the nanosheets. As the doping concentration was further increased to 5%, the nanosheet structure gradually collapsed, forming a secondary network structure with interwoven residual nanosheets (Figure S1d). This was primarily attributed to the strong intercalation effect of high-concentration Zn^{2+} and its directed regulation of crystal growth kinetics. Excessive Zn^{2+} intercalation into the MnO_2 layers not only enhanced interlayer electrostatic bonding, leading to overly dense layer stacking, but also induced significant lattice distortion and localized stress accumulation, which forced the original nanosheets to disintegrate along lattice defects or weak bonding interfaces [30]. Therefore, moderate Zn^{2+} doping resulted in a more uniform and refined network of MnO_2 nanosheets, thereby promoting structural stability [31]. Furthermore, element analysis revealed that K, Mn, O, and Zn were uniformly distributed within the nano-flower-like structure (Figure S2), and no independent ZnO nanoparticle phase was detected. This confirmed that Zn was dispersed within δ-MnO_2 at the atomic level without forming a new phase.

The lattice fringes of δ-MnO_2 and Zn-MnO_2 were analyzed using High-Resolution Transmission Electron Microscope (HRTEM). As shown in Figures 1b and S3b, the lattice fringes at 0.631 and 0.244 nm in the magnified regions corresponded to the (003) and (101) crystal planes of Zn-MnO_2, respectively [32]. These fringes exhibited reduced intensity compared to those of the (003) and (101) crystal planes in δ-MnO_2 (Figures 1a and S3a). This was attributed to Zn^{2+} (0.74 Å), whose ionic radius was smaller than that of the interlayer K^+ (1.38 Å), resulting in partial substitution [30]. The X-ray Diffraction (XRD) results showed that with increasing Zn doping concentration, the characteristic (003) peak shifted toward larger angles, and its intensity decreased (Figure 1c). This may be caused by lattice distortion and defects introduced by Zn doping, leading to reduced crystallinity [25], which was consistent with the HRTEM results. The phases of the sample were analyzed using Rietveld refinement XRD, and the corresponding lattice strain (S) was calculated by Equation (S5) in the supporting information. The refined XRD results confirmed that the Zn-MnO_2 crystal structure was similar to that of δ-MnO_2 (JCPDS No. 52-0556), with no other impurity phases detected (Figures 1d and S4). The weighted residual factor (R_{wp}), residual factor (R_p), and simplified chi-square (χ^2) served as vital parameters for evaluating the quality of the fit following structural refinement in XRD fitting [33,34]. These parameters were calculated through the GSAS-II software to verify the agreement between the experimental results and the XRD fitting results. The values of fitting parameters such as R_{wp}, R_p, and χ^2 were shown in Table S1. The δ-MnO_2 crystal structure (a = 2.849 Å, b = 2.849 Å, and c = 21.536 Å) was constructed from edge-sharing [MnO_6] octahedral layers, with K^+ and H_2O intercalated between the layers [31]. It can be seen that the lattice parameters a, b, and c gradually increased with increasing Zn doping concentration, which could be attributed to the substitution of Mn^{4+} within the layers and K^+ between the layers by Zn^{2+}. Refined XRD calculations obtained S values of 0.13, 0.08, 0.32, and 0.48 for δ-MnO_2 and C-Zn-MnO_2, respectively, confirming that Zn doping induced lattice distortion [24].

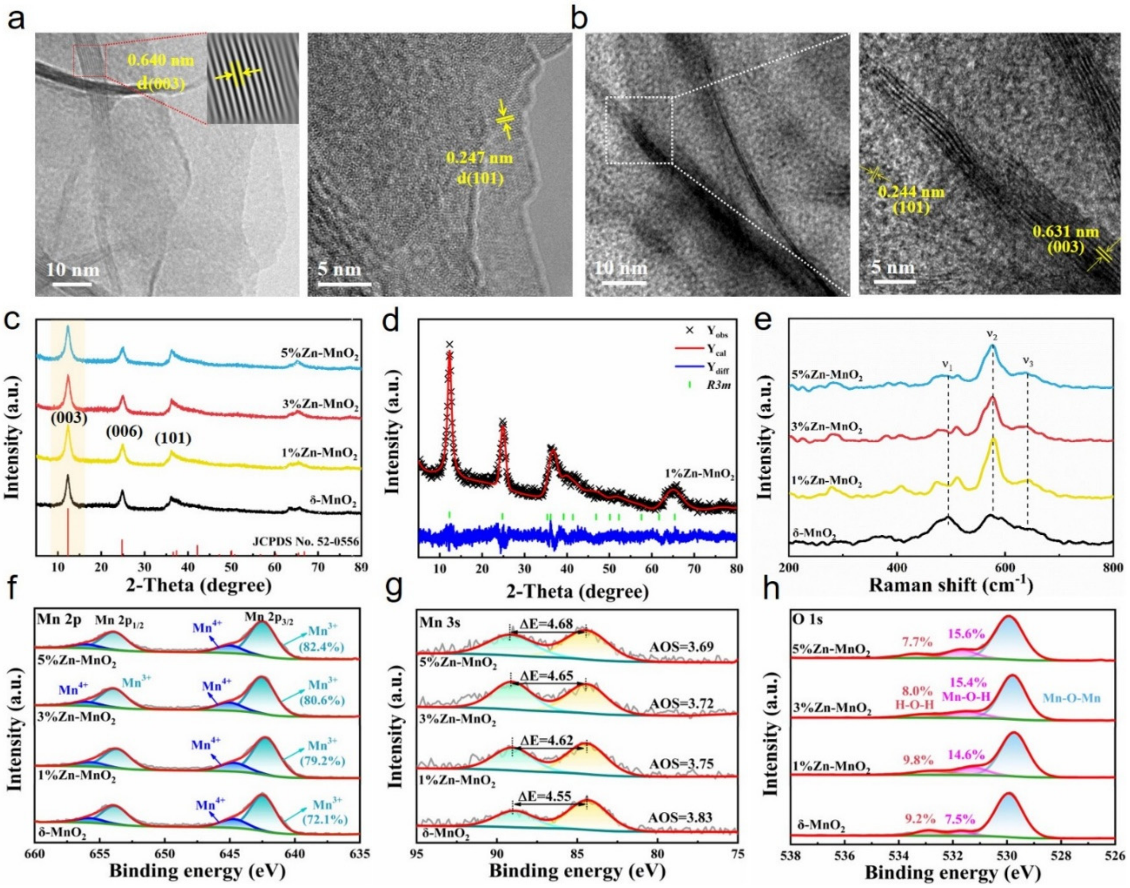

Figure 1. TEM and HRTEM images of (**a**) δ-MnO_2 and (**b**) Zn-MnO_2. (**c**) XRD patterns of samples images. (**d**) Rietveld refined XRD results of 1%Zn-MnO_2. (Experimental data, calculated profiles, allowed Bragg diffraction positions and difference curves are marked by cross, red curves, green vertical bars and a blue line). (**e**) Raman spectrum of δ-MnO_2 and C-Zn-MnO_2. XPS spectrum of (**f**) Mn 2p, (**g**) Mn 3s, and (**h**) O 1s for δ-MnO_2 and Zn-MnO_2.

Figure 1e displayed the Raman analysis results for δ-MnO_2 and C-Zn-MnO_2 (C = 1%, 3%, 5%). characteristic peak intensity shifts near 494 cm^{-1} (ν_1), 576 cm^{-1} (ν_2), and 637 cm^{-1} (ν_3) confirmed the embedding of Zn^{2+}, which led to changes in the lattice structure of MnO_2. The ν_1 peak corresponded to the properties of ions located between the [MnO_6] layers in the base lattice, verifying the presence of the birnessite-type MnO_2 [35]. The ν_2 and ν_3 peaks were attributed to in-plane stretching and symmetric stretching modes of the Mn-O bond within the [MnO_6] units, respectively [36,37]. Compared to δ-MnO_2, the decrease in the intensity of the ν_1 peak indicated that Zn^{2+} substituted for some interlayer K^+ ions, resulting in a reduced interlayer spacing, which suppressed the interlayer vibrational modes and increased the degree of structural disorder. The ν_2 peak exhibited increased intensity and red shift, with the peak intensity rising initially and then decreasing. The substitution of Zn^{2+} for some Mn sites within the layer induced in-plane compressive stress due to the smaller ionic radius of Zn^{2+}, thereby increasing the bond energy of the in-plane Mn-O bonds and making the symmetric stretching vibration mode easier to activate. However, there was no peak at 350 cm^{-1} (Zn-O bond), which proved that Zn^{2+} existed in the interlayer of MnO_2 through electrostatic interactions [38,39].

XPS analysis of the electronic structure of MnO_2 was conducted to further elucidate the causes of lattice distortion in Zn-MnO_2. The XPS full spectrum displayed characteristic peaks for K, Mn, O, C, and Zn (Figure S5a), which were consistent with the EDS analysis results. It can be observed that the signal intensity of K in the C-Zn-MnO_2 samples decreased, indicating that some K^+ between the MnO_2 nanosheets was replaced by Zn^{2+}. The characteristic peaks located at 642.4 eV and 653.8 eV for Mn $2p_{3/2}$ and Mn $2p_{1/2}$ were attributed to Mn^{3+} as shown in Figure 1f [40]. With increasing Zn concentration, the Mn 2p characteristic peaks shifted toward lower binding energies, indicating a decrease in the oxidation state of Mn. The Mn^{3+}/Mn^{4+} ratios in 1% Zn-MnO_2, 3% Zn-MnO_2, and 5% Zn-MnO_2 were 3.81, 4.15, and 4.68, respectively, which were all significantly higher than the 2.58 value of δ-MnO_2. Meanwhile, the splitting energy of the Mn 3s energy level also increased with doping (Figure 1g), and the calculated average oxidation state (AOS) of Mn gradually decreased from 3.83 in δ-MnO_2 to 3.69 in the 5% doped sample. These observations collectively indicated that the substitution of Mn sites in the lattice by Zn^{2+} triggers a charge compensation effect. Some of the Mn^{4+} ions were reduced to Mn^{3+} to maintain electrical neutrality. At the same time, oxygen vacancies were formed, which further exacerbated the local accumulation of electrons and led to lattice expansion. In the O 1s spectra, both the δ-MnO_2 and Zn-MnO_2 samples exhibited three characteristic peaks, corresponding to Mn-O-Mn (529.9 eV), Mn-O-H (531.7 eV), and H-O-H (533.0 eV), respectively [41]. The Mn-O-Mn characteristic peak of MnO_2 gradually shifted toward lower binding energies with increasing Zn doping, reaching its lowest binding energy (529.7 eV) at 1%Zn doping (Figure 1h). Meanwhile, the proportion of surface-adsorbed oxygen increased, which indicated that Zn doping enhanced the electron density around lattice oxygen. Further analysis of the Zn 2p spectrum revealed that the characteristic peaks at 1021.37 eV and 1044.25 eV correspond to Zn $2p_{3/2}$ and Zn $2p_{1/2}$, respectively [42]. The intensity of the Zn 2p characteristic peak at 1021.37 eV shifted toward higher binding energies as the doping concentration increased, confirming that Zn^{2+} doping led to the partial reduction of Mn^{4+} to Mn^{3+}. The larger ionic radius of Mn^{3+} induced lattice expansion, altering the bond lengths and coordination environment around Zn (Figure S5b). As a result, the bonding between Zn and its outer-shell electrons was strengthened and led to significant changes [43].

Further characterization and calculation of the spin configurations of δ-MnO_2 and Zn-MnO_2 were performed by measuring the FC-related magnetic susceptibility. The Curie constants of δ-MnO_2 and Zn-MnO_2 were 1.55 and 1.91, corresponding to effective magnetic moments μ_{eff} of 3.52 and 3.91, respectively (Table S2). These indicated that δ-MnO_2 had three unpaired electrons and Zn-MnO_2 had four unpaired electrons (Figures 2a and S6a). This is due to lattice distortion caused by the introduction of Zn^{2+}, which led to delocalization of more d electrons around the Mn centers [44,45]. As shown in Figure 2b, the hysteresis loops were measured over a magnetic field range of −20 to 20 kOe. The curves for δ-MnO_2 and Zn-MnO_2 displayed similar shapes with no hysteresis, indicating paramagnetic behavior. The calculation and fitting results demonstrated that the magnetic susceptibility of Zn-MnO_2 (5.13×10^{-5}) was significantly higher than that of δ-MnO_2 (4.47×10^{-5}), indicating a transition in the electronic spin state of the Mn centers. The calculated e_g occupation rates for δ-MnO_2 and Zn-MnO_2 were 1.03 and 1.27, respectively (Figure S6b). These results were based on Equations (S6)–(S8) and suggested that Zn-MnO_2 had fewer unoccupied e_g levels [46]. The Electron Paramagnetic Resonance (EPR) spectra in Figure 2c demonstrated that δ-MnO_2 and Zn-MnO_2 displayed strong resonance at g = 2.003 with respect to the center of symmetry [46,47]. The EPR signal peak intensity of Zn-MnO_2 reached 3.037×10^{13} spins/g, which was higher than that of δ-MnO_2 (2.625×10^{13} spins/g). This verified that lattice distortion induced an increase in the number of unpaired electrons in the d orbitals, thereby generating more delocalized d electrons.

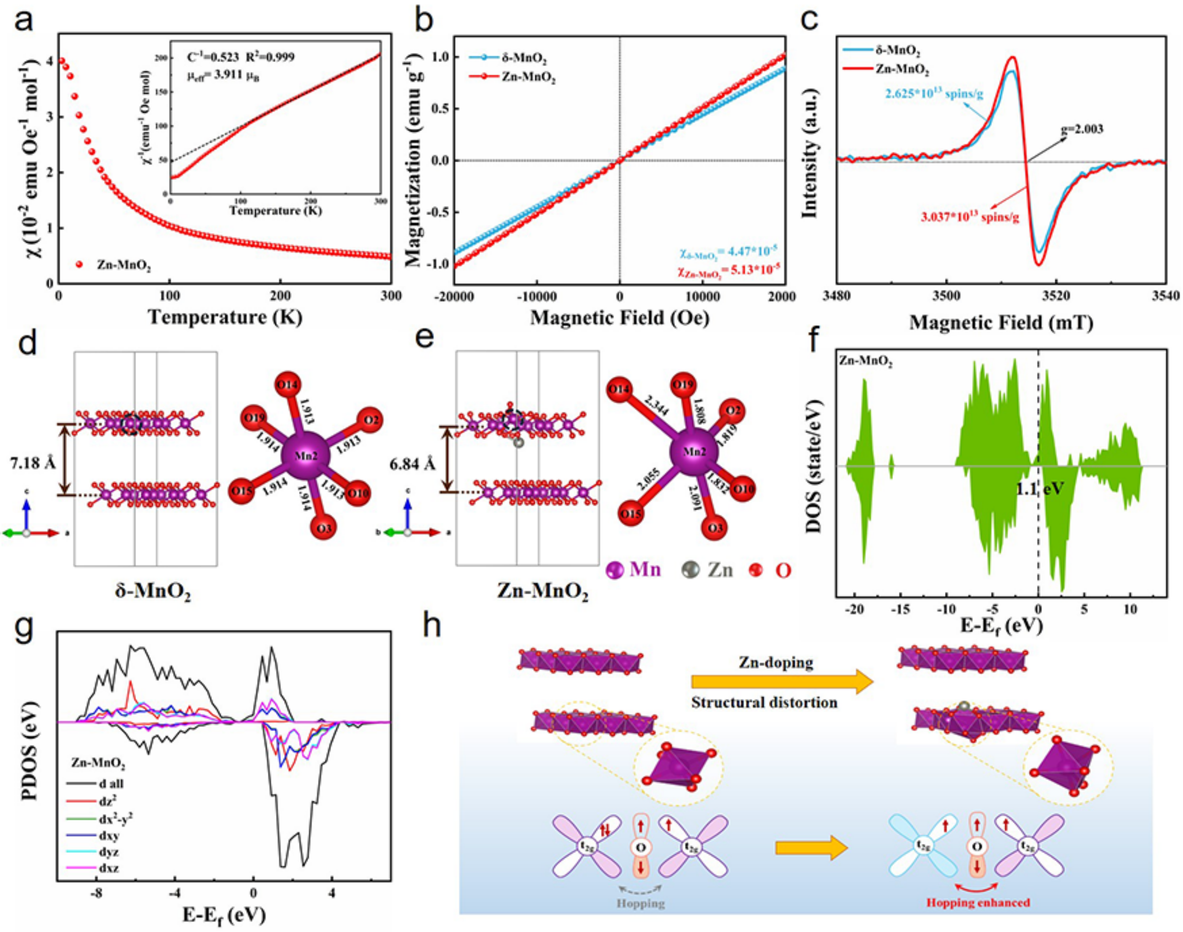

Figure 2. (**a**) Magnetic susceptibility curve of Zn-MnO$_2$ (insert: the plot of inverse susceptibility vs. temperature). (**b**) Magnetic hysteresis loops. (**c**) EPR spectrum of δ-MnO$_2$ and Zn-MnO$_2$. (**d**,**e**) The theoretically optimized structural models of MnO$_2$ and Zn-MnO$_2$. The enlarged Mn-O bond lengths corresponding to the unit cells cycled by black dots. (**f**) DOS of Zn-MnO$_2$. (**g**) The PDOS of different Mn 3d orbitals in Zn-MnO$_2$. (**h**) MnO$_2$ and Zn-MnO$_2$ structural model and schematic diagram of the corresponding t_{2g} orbital modulation electron hopping process.

An atomic structural evolution of Zn-doped MnO$_2$ was obtained through first-principles simulations, including lattice constants and lattice angles, with Zn ions intercalated between layers. The enlarged and optimized unit cell models of δ-MnO$_2$ and Zn-MnO$_2$ were shown in Figure 2d,e. Compared to δ-MnO$_2$, Zn-MnO$_2$ exhibited lattice distortion in its unit cell. Three of the Mn-O bonds are elongated to 1.914 Å (Mn$_2$-O$_{14}$), 2.055 Å (Mn$_2$-O$_{15}$), and 2.091 Å (Mn$_2$-O$_3$), respectively. In contrast, the remaining three Mn-O bonds shortened from 1.913 Å to 1.808 Å (Mn$_2$-O$_{19}$), 1.819 Å (Mn$_2$-O$_2$), and 1.832 Å (Mn$_2$-O$_{10}$). Meanwhile, the layered structure of δ-MnO$_2$ displayed high symmetry with an interlayer spacing of 7.18 Å. With Zn doping into the interlayer, the lattice along the c-axis contracted to 6.84 Å, which was consistent with the XRD and TEM analysis results. The DFT calculation results provided theoretical support for the presence of lattice distortion in Zn-MnO$_2$. Zn doping-induced lattice distortion significantly reduced the bandgap of the material, causing the bandgap value of δ-MnO$_2$ (1.7 eV) to decrease to 1.1 eV in Zn-MnO$_2$ after doping (Figures 2f and S7a). At the same time, the Fermi level (E_F) exhibited a trend of shifting from the top of the valence band to the bottom of the conduction band, which was attributed to the enhanced spin polarization effect caused by lattice distortion [48]. Both the reduced bandgap and the shift in the E_F indicated an increase in the number of delocalized d-electrons in Zn-MnO$_2$, which enhanced electron mobility and contributed to the improvement of the intrinsic electron conductivity of MnO$_2$. The contributions of different 3d partial orbitals of Mn atoms to the total density of states were investigated to further explore the impact of lattice distortion on the electronic structure of MnO$_2$. Partial Density of States (PDOS) analysis revealed that compared to δ-MnO$_2$, the charge distribution in Zn-MnO$_2$ exhibited stronger orbital hybridization characteristics (Figure S7b) [49]. The charge density in Zn-MnO$_2$ was significantly increased near the E_F, indicating a stronger delocalization tendency of its d electrons, consistent with the observations from the PDOS analysis (Figure 2g). Table S3 showed the electron occupation rates of the e_g and t_{2g} orbitals in the Mn 3d. The electron occupancy of the e_g orbital in Zn-MnO$_2$ (39.61%) was slightly higher than that of δ-MnO$_2$ (39.16%). Although the numerical change was small, the upward trend was quite pronounced. This increase directly demonstrated the enhanced degree of electron delocalization, indicating the presence of more delocalized d electrons in Zn-MnO_2. This theoretical calculation result was consistent with the analytical conclusions regarding electron delocalization and spin states derived from the magnetic measurements described above.

Zn doping-induced lattice distortion in MnO_2 is the core mechanism for modulating the electronic spin states of the Mn centers while simultaneously optimizing charge storage and HER performance (Figure 2h). This approach is consistent with the emerging strategy of spin-state engineering, which directly influences orbital occupancy and reaction kinetics to overcome the limitations of conventional electronic structure modulation [50]. Due to the larger radius of the Zn^{2+} ion compared to that of Mn^{4+} (0.53 Å), its substitution for Mn^{4+} within the [MnO_6] octahedral layer results in significant lattice distortion. The structural change not only alleviates lattice stress during the ion incorporation process but also alters the local symmetry of the [MnO_6] octahedral field, leading to a shift in the splitting of Mn 3d orbital energy levels. This results in an increase in the electron occupancy of the e_g orbitals while reducing the electron occupancy of the t_{2g} orbitals, thereby enhancing the spin polarization effect [51,52]. The filling state of the t_{2g} orbitals directly influenced the charge transfer dynamics. The fully occupied t_{2g} orbitals in MnO_2 reinforce electron localization, suppressing O_2^--mediated electron hopping between Mn^{3+} and Mn^{4+} and hindering charge transfer. In contrast, the moderate distortion caused by Zn doping broke the saturated occupation of the t_{2g} orbitals, lowered the energy barrier for electronic transitions and promoted the delocalization of d electrons [53]. Consequently, the bandgap of Zn-MnO_2 was significantly reduced and the conduction band shifted toward the energy front, while the Mn 3d orbitals exhibited stronger hybridization characteristics and charge density distribution near the Fermi surface, indicating the formation of delocalized electronic pathways. There are two primary effects of modulating the electronic structure. On the one hand, the increased contribution from the e_g orbitals not only enhanced the adsorption ability for ions and optimized the binding strength during the redox process, but also expanded the unit cell structure to accelerate ion diffusion kinetics [54,55]. On the other hand, adjusting the occupation state of the t_{2g} orbitals can directly reduce the adsorption energy of the H* intermediate to promote the desorption process, and enhance the dissociation kinetics of water molecules through the spin-polarization effect to improve the catalytic activity of the HER [56]. Moreover, delocalized electronic networks can optimize the efficiency of internal electron transport to increase the rate of charge transfer between active sites and reaction interfaces and accelerate the reaction kinetics [57].

The electrochemical performance of δ-MnO_2 and C-Zn-MnO_2 with different Zn doping concentrations was evaluated in 1 M Li_2SO_4 electrolyte using the three-electrode system. Figure S8a displayed the Cyclic voltammetry (CV) curves in the −0.2 to 1 V voltage window at a scan rate of 80 mV s^{-1}. δ-MnO_2 demonstrated lower integrated areas and weaker redox peak intensities due to limited charge storage sites, whereas the CV closed-loop areas for 1%, 3%, and 5%Zn-MnO_2 were significantly expanded. In particular, the 1%Zn-MnO_2 electrode revealed the highest response current and integrated area, which was attributed to Zn^{2+} doping-induced lattice distortion in MnO_2. By regulating the valence state of Mn, the density of active sites and surface adsorption capacity were enhanced, thereby significantly increasing the pseudocapacitive contribution. The Galvanostatic charge-discharge (GCD) test results were consistent with the CV analysis results (Figure 3a). The performance of the doped samples improved at the current density of 0.5 A g^{-1}, with 1% as the optimal doping concentration. The discharge time of 1%Zn-MnO_2 was approximately 1.2 times longer than that of δ-MnO_2, with the specific capacitance increasing from the initial 155.29 F g^{-1} to 192.04 F g^{-1}. The well-symmetrical triangular curve indicated efficient charge storage kinetics and reversibility. However, over-doping with more than 3% Zn may exacerbate lattice distortion, which led to the masking of active sites.

As shown in Figure S8b, the kinetic characteristics were further analyzed by Electrochemical impedance spectrum (EIS) within the frequency range of 0.01 Hz to 100 kHz. The data revealed that the R_{ct} of the C-Zn-MnO_2 electrodes was lower than the R_{ct} of δ-MnO_2 (2.15 Ω), with the 1%Zn-MnO_2 electrode exhibiting the lowest R_{ct} (1.74 Ω) (Table S4). The vertical slope in the low-frequency region was steeper, indicating lower interfacial charge transfer resistance and a faster ion diffusion rate. This kinetic advantage was particularly pronounced in rate performance testing (Figure 3b), where the 1%Zn-MnO_2 electrode maintained a specific capacitance of 42.7 F g^{-1} at a current density of 8 A g^{-1}, which was higher than the 14 F g^{-1} of δ-MnO_2. Although the 3% and 5%high-Zn-doped samples also exhibited higher specific capacitance than δ-MnO_2 at high current densities, their rate performance displayed significantly accelerated degradation, which may be attributed to structural stress accumulation caused by excessive doping. Figure S8c showed the CV test results of the Zn-MnO_2 electrode at different scan rates. All curves exhibited nearly rectangular pseudocapacitive characteristics, and the curve shapes remain stable when scan rates increase. The current response was significantly enhanced, indicating the excellent capacitive properties and rapid charge-discharge capabilities of the Zn-MnO_2 [58]. The b values obtained for δ-MnO_2 were 0.47 and 0.53, while those for Zn-MnO_2 were 0.61 and 0.66 (Figures 3c and S8d), confirming that its energy storage mechanism relies primarily on diffusion control [59]. However, Zn-MnO_2 exhibited a greater degree of surface capacitance contributions, where the yellow shaded area represented the surface capacitance contribution corresponding to the CV curve at 10 mV s^{-1}, and the remaining unshaded area represents the diffusion-controlled region (Figures S8e and S8f) [32]. As shown in Figure 3d, the contribution of surface capacitance for the Zn-MnO_2 electrode in the scan rate range of 10–80 mV s^{-1} increased from 23.08%, 30.44%, 37.4%, and 50.32% to 67.9%. Compared to the surface capacitance of δ-MnO_2, the increase indicates that the electron/ion transport kinetics of the electrode had been optimized.

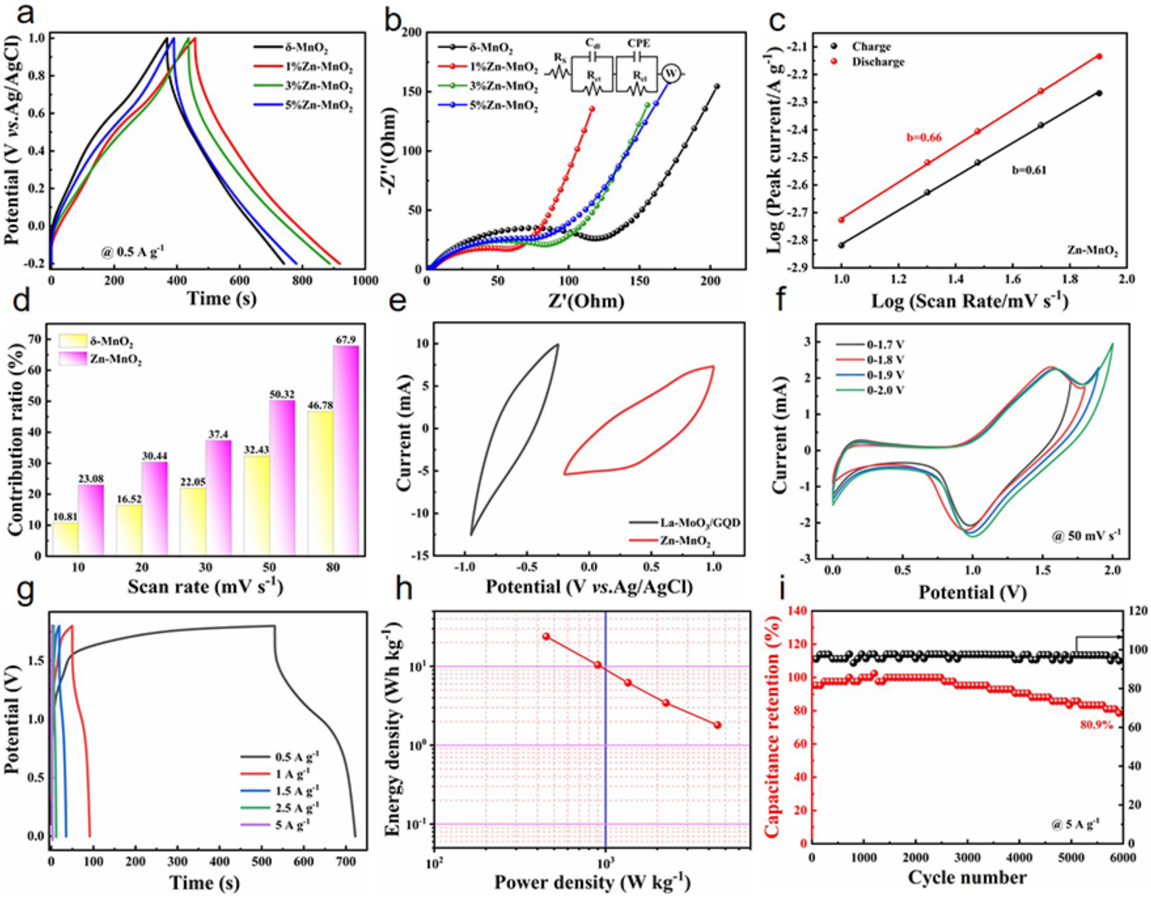

Figure 3. (**a**) GCD curves of samples at 0.5 A g^{-1}. (**b**) Nyquist plots. (**c**) Power law relationship of Zn-MnO_2 electrode at different scanning rates. (**d**) Contribution ratio of the capacitance-controlled for δ-MnO_2 and C-Zn-MnO_2 at different scan rates. Electrochemical performance of Zn-MnO_2//La-MoO_3/GQDs asymmetric supercapacitors: (**e**) CV curves of the negative electrode and positive electrode at a scan rate of 80 mV s^{-1}. (**f**) CV curves of the device for varying potential ranges at the scan rate of 50 mV s^{-1}. (**g**) GCD curves at current density from 0.5 to 5 A g^{-1}. (**h**) Ragone plot. (**i**) Cyclic stabilities after 6000 cycles.

An asymmetric supercapacitor was assembled using Zn-MnO_2 as the cathode and La-MoO_3/GQD as the anode to demonstrate the good electrochemical performance of the Zn-MnO_2. Figure S9a showed a schematic diagram of the device. The CV curves of Zn-MnO_2 and La-MoO_3/GQD were measured at scan rates of 80 mV s^{-1} within the voltage ranges of -0.2 V to 1 V and -0.95 V to -0.25 V, respectively (Figure 3e). CV curves of the Zn-MnO_2//La-MoO_3/GQD device were obtained at different potentials using a constant scan rate of 50 mV s^{-1} (Figure 3f). These curves indicated that the potential of the Zn-MnO_2//La-MoO_3/GQD device can reach 2.0 V, and no significant polarization was observed at 1.8 V. Figure S9b displayed CV curves recorded at scan rates ranging from 10 to 200 mV s^{-1} within a potential window of 1.8 V. A decrease in scan rate resulted in more pronounced redox peaks in the CV curves, indicating high reversibility. When the scan rate was increased to 200 mV s^{-1}, the CV curve exhibited minimal distortion, indicating a high I-V response of the device. The capacitive performance of the device was verified through GCD testing at various current densities [60]. The maximum specific capacitance of 53.1 F g^{-1} was measured at a current density of 0.5 A g^{-1} (Figure 3g). The resistance characteristics of the device were evaluated by EIS over the frequency range of 0.01 Hz to 100 kHz. Figure S9c showed the Nyquist plot, where the intersection of the high-frequency region with the real axis indicated an internal resistance of approximately

1.36 Ω. Figure S9d illustrated the relationship between the phase angle of the asymmetric supercapacitor and frequency. The phase angle in the low-frequency region reached approximately 50°, reflecting excellent capacitive performance and stability. At a power density of 450 W kg^{-1}, the device achieved an energy density of 23.9 Wh kg^{-1}, which was superior to previously reported asymmetric supercapacitors, as shown in Figure 3h and Table S5. Charge-discharge cycle stability tests were conducted to evaluate the potential for practical applications. After 6000 cycles at a current density of 5 A g^{-1}, the device exhibited a capacitance retention rate of 80.9%, indicating that it can operate stably within a working voltage window of 1.8 V (Figure 3i).

A systematic evaluation of the HER performance of δ-MnO_2 and C-Zn-MnO_2 with different Zn doping concentrations (1%, 3%, 5%) was conducted in a 1 M KOH electrolyte. As shown in Figure 4a, Linear Sweep Voltammetry (LSV) testing revealed that the HER activity of the C-Zn-MnO_2 series electrodes was significantly enhanced compared to δ-MnO_2. The polarization curve of the 1%Zn-MnO_2 electrode exhibited the lowest overpotential. As shown in Figure 4b, the overpotentials at a current density of 10 mA cm^{-2} for δ-MnO_2, 1%Zn-MnO_2, 3%Zn-MnO_2, and 5%Zn-MnO_2 were 232 mV, 161 mV, 171 mV, and 177 mV, respectively. Tafel slope analysis revealed differences in reaction kinetics (Figure 4c). Compared with the δ-MnO_2 electrode (103 mV dec^{-1}), the Tafel slopes of the Zn-MnO_2 electrodes were all reduced. The 1%Zn-MnO_2 exhibited the smallest Tafel slope, which was 85 mV dec^{-1}, indicating that the HER process at the 1%Zn-MnO_2 tended toward the Volmer-Heyrovsky pathway, with the Volmer reaction acting as the rate-determining step. The semicircular feature observed in the Nyquist plot reflects the efficient charge transfer process between the electrode material and the electrolyte (Figure 4d). The R_s values of the Zn-doped samples were lower than those of δ-MnO_2, indicating that the overall conductivity of the electrode has been optimized (Table S6). The 1%Zn-MnO_2 exhibited the lowest R_{ct} of 4.97 Ω among all samples, indicating high HER activity due to rapid charge transfer to catalytic active sites. In contrast, the δ-MnO_2 showed a higher R_{ct} of 15.62 Ω, suggesting lower HER activity, a result consistent with the conclusions from the polarization curves. The CV curves for all samples are shown in Figure S10, and the double-layer capacitance (C_{dl}) was calculated. The C_{dl} of the 1%Zn-MnO_2 electrode was 7.8 mF cm^{-2}, which was 1.6 times that of the δ-MnO_2 (4.8 mF cm^{-2}), confirming that its surface exposed a greater abundance of active sites (Figure 4e). Compared to the 3% and 5%Zn-MnO_2 electrodes, which demonstrated C_{dl} values of 6.1 mF cm^{-2} and 5.8 mF cm^{-2}, respectively. Furthermore, a comparison was made with current MnO_2-based catalysts, as shown in Table S7. These results indicated that 1%Zn doping represented the optimal condition for achieving a high density of active sites. The 1%Zn-MnO_2 was subjected to 5000 CV cycles in the non-Faradaic region (Figure 4f). The LSV curves before and after cycling showed significant agreement, which demonstrated the excellent cyclic stability of the electrode.

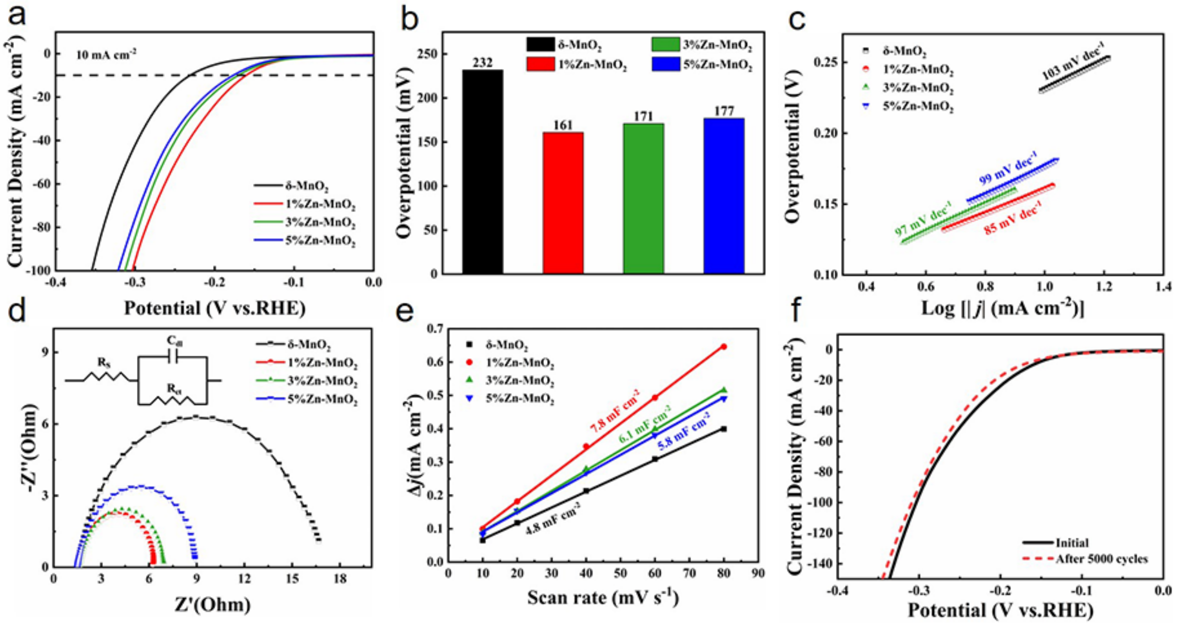

Figure 4. (**a**) LSV curves of δ-MnO_2 and C-Zn-MnO_2. (**b**) Overpotential (η_{10}). (**c**) Tafel slopes. (**d**) Nyquist plot (insert: the equivalent). (**e**) Linearly fitting curves of the capacitive current as a function of scan rate. (**f**) LSV curve of Zn-MnO_2 after 5000 CV cycles.

4. Conclusions

In this work, we modulated the spin states of MnO_2 using a Zn-doping-induced lattice distortion strategy to enhance its charge storage capacity and HER. Zn^{2+} doping induced lattice distortion in MnO_2 and expanded its unit cell volume, significantly increasing the electron occupation of the e_g orbitals by altering the splitting energy of the $[MnO_6]$ octahedral field. This enhanced the spin polarization effect and promoted d-electron delocalization, reducing the bandgap of MnO_2 from 1.7 eV to 1.1 eV and significantly improving its intrinsic electronic conductivity. Appropriate lattice distortion modulates the spin states of MnO_2, transforming its t_{2g} orbitals from a fully occupied state to a half-filled state. This facilitates electronic hopping in the t_{2g} orbitals and accelerates the O_2^--mediated charge transfer process, thereby significantly lowering the reaction barrier for the HER. In addition, the increase in the number of delocalized electrons and the expansion of the unit cell volume effectively promote ion diffusion, enabling this asymmetric supercapacitor device to exhibit a high energy density of 23.9 Wh kg^{-1} and excellent cycling stability of 80.9%. Concurrently, the enhanced charge transfer kinetics and increased active site density drove the improvement in HER activity, reducing the reaction potential from 232 mV to 161 mV at a current density of 10 mA cm^{-2}.

Supplementary Materials

The additional data and information can be downloaded at: https://media.sciltp.com/articles/others/2606121511328814/eChem-26040207-SM-final.pdf. References [61–71] are cited in Supplementary Materials.

Author Contributions

J.L.: Writing—original draft, Investigation, Data curation, Visualization, Funding acquisition. X.Z.: Methodology, Formal analysis, Funding acquisition. X.W.: Investigation, Data curation. J.H.: Writing—review & editing. X.L.: Supervision, Conceptualization. R.F.: Funding acquisition, Visualization. Y.G.: Conceptualization, Funding acquisition, Writing—review & editing. All authors have read and agreed to the published version of the manuscript.

Funding

This work was supported by the Daqingshan Laboratory Scientific and Technological Support Program (2025KYPT0187), 2025 Autonomous Region University Basic Scientific Research Business Expenses Project-Inner Mongolia University of Technology: Improving Basic Scientific Research Capabilities of Outstanding On-Campus Students (ZTY2025015).

Data Availability Statement

Data will be made available on request.

Conflicts of Interest

The authors declare no conflict of interest.

Use of AI and AI-Assisted Technologies

No AI tools were utilized for this paper.

References

1. Ayub, M.N.; Alotaibi, A.N.; Rabbee, M.F.; et al. Harnessing 2D Nanostructure Inorganic Materials for Efficient and Sustainable Supercapacitor Energy Storage. *Chem.-Asian J.* **2026**, *21*, e70558. https://doi.org/10.1002/asia.70558.
2. Chu, M.; Zhang, T.; Song, P.; et al. Unique Structural Features of Polyoxometalates for Efficient Alkaline Hydrogen-Evolution Reaction. *ChemSusChem* **2026**, *19*, e202502761. https://doi.org/10.1002/cssc.202502761.
3. Nair, A.R.; Vetrikarasan, T.B.; Bulakhe, R.; et al. Morphology-controlled and nitrate anion-driven growth of δ-MnO_2 for reduced graphene oxide and $Ti_3C_2T_x$ MXene-based high-energy-density flexible supercapacitor. *J. Power Sources* **2026**, *677*, 239980.
4. Hua, H.; Zhang, Z.; Liu, G.; et al. Erbium-doped MnO_2 for degrading polyethylene terephthalate linking to hydrogen evolution. *Int. J. Hydrogen Energy* **2025**, *145*, 542–547.
5. Yuan, Y.; He, K.; Lu, J. Structure–Property Interplay within Microporous Manganese Dioxide Tunnels For Sustainable Energy Storage. *Angew. Chem. Int. Ed.* **2024**, *63*, e202316055. https://doi.org/10.1002/anie.202316055.

6. Chen, Y.-C.; Liu, B.-Y.; Feng, Y.; et al. Light–induced antibonding orbital occupancy accelerates ion intercalation kinetics for enhanced capacitance of photo–rechargeable supercapacitor based on MnO2/ZnO electrode. *J. Energy Storage* **2026**, *152*, 120610. https://doi.org/10.1016/j.est.2026.120610.
7. Kore, A.E.; Kore, E.K.; Gavande, S.S.; et al. Impact of various aqueous electrolytes on the electrochemical performance of Zinc-doped δ-MnO_2 nanowires as electrode material for supercapacitor device applications. *J. Alloys Compd.* **2025**, *1042*, 184116. https://doi.org/10.1016/j.jallcom.2025.184116.
8. Zhu, Y.-P.; Xia, C.; Lei, Y.; et al. Solubility contrast strategy for enhancing intercalation pseudocapacitance in layered MnO_2 electrodes. *Nano Energy* **2019**, *56*, 357–364. https://doi.org/10.1016/j.nanoen.2018.11.063.
9. Wang, P.; Yan, Y.; Cao, J.; et al. Surface activation towards manganese dioxide nanosheet arrays via plasma engineering as cathode and anode for efficient water splitting. *J. Colloid Interface Sci.* **2021**, *586*, 95–102. https://doi.org/10.1016/j.jcis.2020.10.073.
10. Li, X.; Yang, J.; Zhang, F.; et al. Orbital-Level Electronic Modulation of MnO_2 via Interfacial Built-In Electric Fields: Breaking the Jahn–Teller Distortion Cycle for Ultra-Durable Hybrid Capacitive Deionization. *Small* **2025**, *21*, 2505300. https://doi.org/10.1002/smll.202505300.
11. Lin, Y.; Luo, S.; Li, P.; et al. Introducing strong metal–oxygen bonds to suppress the Jahn-Teller effect and enhance the structural stability of Ni/Co-free Mn-based layered oxide cathodes for potassium-ion batteries. *J. Energy Chem.* **2025**, *101*, 713–722. https://doi.org/10.1016/j.jechem.2024.10.017.
12. Zhou, S.; Liao, J.; Yu, C.; et al. Generality Rules and Synergistic Effect of Mitigating the Jahn–Teller Effect by Multisites Compositionally Complex Doping. *ACS Nano* **2024**, *18*, 35356–35367. https://doi.org/10.1021/acsnano.4c12022.
13. Gong, S.; Yang, J.Y.; Chen, G.; et al. Spin State Manipulation: A Key to High-Efficiency Electrocatalytic Oxygen Evolution Reaction. *ACS Appl. Mater. Interfaces* **2026**, *18*, 17313–17355. https://doi.org/10.1021/acsami.5c24044.
14. Zhang, X.M.; Zhang, X.Y.; Wang, X.B.; et al. Engineering spin states of metal sites toward advanced lithium-sulfur batteries. *Energy Environ. Sci.* **2025**, *18*, 3553–3567. https://doi.org/10.1039/d4ee05582a.
15. Xu, B.-C.; Miao, Y.-P.; Mao, M.-Q.; et al. Heterophase junction engineering-induced Co spin-state modulation of $CoSe_2$ for large-current hydrogen evolution reaction. *Rare Met.* **2024**, *43*, 2660–2670. https://doi.org/10.1007/s12598-024-02624-w.
16. Wang, T.; Wang, Z.H.; Gao, X.T.; et al. Spin-states modulated single-atom catalysts for boosted polysulfides conversion in lithium-sulfur batteries. *J. Energy Chem.* **2026**, *117*, 694–702. https://doi.org/10.1016/j.jechem.2026.03.003.
17. Yang, R.A.; Zhang, G.L.; Yu, H.; et al. Electrocatalysis synergism motivated by low energy d-orbitals at high spin state for long-lifespan Li-O2 batteries. *Appl. Catal. B-Environ. Energy* **2026**, *381*, 125831. https://doi.org/10.1016/j.apcatb.2025.125831.
18. Li, S.; Yue, F.; Tan, H.; et al. Tailoring the Effects of Spin State and Intermediate Hydrogen Adsorption on NiPt/Ni Bridge Sites toward Robust Acidic Water Electrolysis. *Nano Lett.* **2025**, *25*, 13956–13964. https://doi.org/10.1021/acs.nanolett.5c04035.
19. Du, X.B.W.; Zheng, X.Z.; Lu, B.; et al. Rare-earth-driven spin-state engineering activates catalyst supports for durable low-Ir acidic water electrolysis. *Appl. Catal. B-Environ. Energy* **2026**, *389*, 126598. https://doi.org/10.1016/j.apcatb.2026.126598.
20. Gu, J.H.; He, L.; Wang, X.; et al. Tuning TM-O Bond Covalency to Boost Cationic Activity and Reversibility of $Na_4Fe_{1.5}Mn_{1.5}(PO_4)_2P_2O_7$. *Nano Lett.* **2025**, *25*, 7826–7834. https://doi.org/10.1021/acs.nanolett.5c00931.
21. Nguyen, J.; Lee, Y.; Yang, Y. Suppression of High Spin State of Mn for the Improvement of Mn-Based Materials in Rechargeable Batteries. *Small* **2024**, *22*, 2410453. https://doi.org/10.1002/smll.202410453.
22. Liu, Y.; Kong, L.S.; Li, H.B.; et al. Atomically dispersed Zn-N_3 sites boost ROS production for enhanced oxidase-like antibacterial performance. *Colloids Surf. A-Physicochem. Eng. Asp.* **2026**, *736*, 139650. https://doi.org/10.1016/j.colsurfa.2026.139650.
23. Oliveira, R.A.; Lavela, P.; Bomio, M.R.D.; et al. Engineering Zn-doped $NiCo_2O_4$ spinels for enhanced charge storage in high-performance asymmetric supercapacitors. *J. Mater. Sci.* **2026**, *61*, 11097–11118. https://doi.org/10.1007/s10853-026-12554-w.
24. Li, G.; Yu, W.; Diao, Q.; et al. Zn-Doped Hollow Cubic MnO_2 as a High-Performance Cathode Material for Zn Ion Batteries. *ChemPhysChem* **2025**, *26*, e202400860. https://doi.org/10.1002/cphc.202400860.
25. Abbas, S.; Bokhari, T.H.; Zafar, A.; et al. Zn doping induces rich oxygen vacancies in δ-MnO_2 flower-like nanostructures for impressive energy density coin cell supercapacitor. *J. Energy Storage* **2024**, *87*, 111455. https://doi.org/10.1016/j.est.2024.111455.
26. Xie, J.; Liu, Q.; Li, S.; et al. Enhancing Intrinsic Reactivity and Durability of Zn-Doped Cobalt Carbonate Hydroxide via d-d Interaction Modulation for Alkaline Zinc Batteries. *Adv. Funct. Mater.* **2025**, *n/a*, e10065. https://doi.org/10.1002/adfm.202510065.
27. Ma, X.; Qi, N.; Zhang, M. First-principles investigation of Zn-doped β-Ga_2O_3: Electronic, optoelectronic, and thermodynamic properties. *Phys. B Condens. Matter* **2025**, *715*, 417557. https://doi.org/10.1016/j.physb.2025.417557.
28. Kresse, G.; Furthmüller, J.; Hafner, J. Theory of the crystal structures of selenium and tellurium: The effect of generalized-gradient corrections to the local-density approximation. *Phys. Rev. B* **1994**, *50*, 13181–13185. https://doi.org/

10.1103/PhysRevB.50.13181.

29. Wang, Y.; Quan, H.; Zhang, Q.; et al. Enhanced Oxygen Vacancies of δ-MnO_2 Nanosheets on Carbon Cloth via Fast Zn^{2+} Intercalation for Supercapacitor Electrodes with High Mass Loading. *ACS Appl. Nano Mater.* **2024**, *7*, 27988–27997. https://doi.org/10.1021/acsanm.4c01620.
30. Chacón-Borrero, J.; Chang, X.Q.; Min, Z.W.; et al. Boosting high-loading zinc-ion battery performance: Zn-Doped δ-MnO2 cathodes to promote Zn^{2+} storage. *Energy Storage Mater.* **2025**, *81*, 104486. https://doi.org/10.1016/j.ensm.2025.104486.
31. Zhao, W.; Fee, J.; Khanna, H.; et al. A two-electron transfer mechanism of the Zn-doped δ-MnO_2 cathode toward aqueous Zn-ion batteries with ultrahigh capacity. *J. Mater. Chem. A* **2022**, *10*, 6762–6771. https://doi.org/10.1039/D1TA10864F.
32. Quan, J.H.; Lin, H.X.; Li, H.Y. Zn Doping Strategy to Suppress the Jahn-Teller Effect to Stabilize Mn-Based Layered Oxide Cathode toward High-Performance Potassium Ion Batteries. *Small* **2024**, *20*, 2403065. https://doi.org/10.1002/smll.202403065.
33. Xiao, Y.P.; Hu, Q.B.; Fan, Y.D.; et al. The effects of MnO_2 doping on the structure, dielectric properties and oxygen vacancies of 82$NaNbO_3$-18$CaTiO_3$ lead-free ceramics. *Solid State Commun.* **2026**, *409*, 116278. https://doi.org/10.1016/j.ssc.2025.116278.
34. Amarray, A.; Salmi, M.; Oubla, M.; et al. Reduction of cadmium content in 29% and 54% P_2O_5 phosphoric acid by manganese oxide material birnessite-type Na-MnO_2. *Desalination* **2023**, *560*, 116677. https://doi.org/10.1016/j.desal.2023.116677.
35. Kim, H.-m.; Choi, J.-y.; Cha, B.-c.; et al. Effect of mixed phase with shape control on lithium ions transport during conversion reaction in the manganese oxide anode. *Appl. Surf. Sci.* **2025**, *688*, 162374. https://doi.org/10.1016/j.apsusc.2025.162374.
36. Yang, L.; Cheng, S.; Wang, J.; et al. Investigation into the origin of high stability of δ-MnO_2 pseudo-capacitive electrode using operando Raman spectroscopy. *Nano Energy* **2016**, *30*, 293–302. https://doi.org/10.1016/j.nanoen.2016.10.018.
37. Bai, H.; Liang, S.; Wei, T.; et al. Enhanced pseudo-capacitance and rate performance of amorphous MnO_2 for supercapacitor by high Na doping and structural water content. *J. Power Sources* **2022**, *523*, 231032. https://doi.org/10.1016/j.jpowsour.2022.231032.
38. Yao, M.; Ji, X.; Chou, T.-F.; et al. Simple and Cost-Effective Approach To Dramatically Enhance the Durability and Capability of a Layered δ-MnO_2 Based Electrode for Pseudocapacitors: A Practical Electrochemical Test and Mechanistic Revealing. *ACS Appl. Energ. Mater.* **2019**, *2*, 2743–2750. https://doi.org/10.1021/acsaem.9b00075.
39. Nakayama, M.; Konishi, S.; Tagashira, H.; et al. Electrochemical Synthesis of Layered Manganese Oxides Intercalated with Tetraalkylammonium Ions. *Langmuir* **2005**, *21*, 354–359. https://doi.org/10.1021/la048173f.
40. Shimna, M.; Mohanty, S. Enhanced electrochemical performance of ultrathin Mo-doped MnO_2 via one-pot hydrothermal synthesis for supercapacitor applications. *Curr. Appl. Phys.* **2026**, *86*, 40–52. https://doi.org/10.1016/j.cap.2026.02.010.
41. Zhang, S.; Ren, S.; Wei, M.; et al. Facile fabrication of bagasse porous carbon@MnO_2 nanowire heterostructures with synergistic effects for high-performance asymmetric supercapacitors. *J. Phys. Chem. Solids* **2026**, *214*, 113663. https://doi.org/10.1016/j.jpcs.2026.113663.
42. Wu, J.; Raza, W.; Wang, P.; et al. Zn-doped MnO_2 ultrathin nanosheets with rich defects for high performance aqueous supercapacitors. *Electrochim. Acta* **2022**, *418*, 140339. https://doi.org/10.1016/j.electacta.2022.140339.
43. He, S.; Mo, Z.; Shuai, C.; et al. Pre-intercalation δ-MnO_2 Zinc-ion hybrid supercapacitor with high energy storage and Ultra-long cycle life. *Appl. Surf. Sci.* **2022**, *577*, 151904. https://doi.org/10.1016/j.apsusc.2021.151904.
44. Wang, Y.J.; Cheng, W.Z.; Yuan, P.F.; et al. Boosting Nitrogen Reduction to Ammonia on FeN4 Sites by Atomic Spin Regulation. *Adv. Sci.* **2021**, *8*, 2102915. https://doi.org/10.1002/advs.202102915.
45. Xue, D.P.; Yuan, P.F.; Jiang, S.; et al. Altering the spin state of Fe-N-C through ligand field modulation of single-atom sites boosts the oxygen reduction reaction. *Nano Energy* **2023**, *105*, 108020. https://doi.org/10.1016/j.nanoen.2022.108020.
46. Gao, X.; Fu, W.; Sun, Y.; et al. Half-disturbed spin desalination: Asymmetric high-spin states in MnO_2 accelerate charge transfer in capacitive deionization. *Desalination* **2024**, *583*, 117739. https://doi.org/10.1016/j.desal.2024.117739.
47. Fu, W.J.; Li, J.X.; Liu, Y.M.; et al. Asymmetric oxygen vacancies in Cu-Ov-Mn units boost charge transfer in MnO_2 for enhanced hybrid capacitive deionization efficiency. *Desalination* **2025**, *613*, 119000. https://doi.org/10.1016/j.desal.2025.119000.
48. Ma, J.; Li, C.; Ji, Q.Q.; et al. V-Induced Low-Spin State Mn3+Suppresses Jahn-Teller Distortion for High-Performance Aqueous Zinc Ion Batteries. *Angew. Chem.-Int. Ed.* **2025**, *64*, e202513148. https://doi.org/10.1002/anie.202513148.
49. Yan, Y.X.; Zhou, J.Y.; Ren, H.D.; et al. Promoting Mn^{3+} Spin-State Transitions from t2g to eg through Ni Doping in Antiperovskite CuNMn3 for Highly Efficient Ammonia Synthesis. *J. Phys. Chem. Lett.* **2025**, *16*, 5025–5033. https://doi.org/10.1021/acs.jpclett.5c00563.
50. Kousar, N.; Patil, G.; Kumbara, A.C.; et al. Engineering of abundant metal complexes for electrochemical water splitting. *Dalton Trans.* **2025**, *54*, 12714–12736. https://doi.org/10.1039/D5DT01438G.
51. Zhou, H.Q.; Li, S.D.; Wei, J.Y.; et al. Mitigating Jahn-Teller distortion in Mn-based layered potassium-ion battery cathodes via controlled lattice distortion. *Chem. Eng. J.* **2026**, *530*, 173573. https://doi.org/10.1016/j.cej.2026.173573.
52. Liang, N.; Zhu, Q.; Jiang, M.P.; et al. Self-Aligned $BiFeO_3$ Polarization Vector Induced by MnO6 Octahedral Jahn-Teller Distortion for Enhanced Photocatalytic CO2 Reduction. *J. Am. Chem. Soc.* **2025**, *147*, 43380–43390. https://doi.org/10.1021/jacs.5c10006.
53. Yao, S.; Zhao, R.; Wang, S.; et al. Ni-doping induced structure distortion of MnO_2 for highly efficient Na^+ storage. *Chem.*

Eng. J. **2022**, *429*, 132521. https://doi.org/10.1016/j.cej.2021.132521.

54. Yao, S.; Wang, S.; Liu, R.; et al. Delocalizing the d-electrons spin states of Mn site in MnO_2 for anion-intercalation energy storage. *Nano Energy* **2022**, *99*, 107391. https://doi.org/10.1016/j.nanoen.2022.107391.
55. Wu, L.L.; He, Y.C.; Zhang, B.; et al. Lattice distortion-induced e_g* band broadening of a nickel-based electrocatalyst for boosting electrocatalytic PBS plastic upcycling. *Appl. Catal. B-Environ. Energy* **2026**, *391*, 126678. https://doi.org/10.1016/j.apcatb.2026.126678.
56. Guo, M.M.; Han, X.D.; Feng, H.; et al. Spin-state-regulated dual-metal orbital engineering in heterostructured nanosheets for d-band center-optimized electrocatalytic water splitting. *J. Colloid Interface Sci.* **2025**, *696*, 137850. https://doi.org/10.1016/j.jcis.2025.137850.
57. Wang, C.J.; Yang, Y.Q.; Zheng, J.L.; et al. Magnetic Field-Driven Spin State Transformation in Promoting the Catalytic Activity of Doped Single-Atom for Hydrogen Evolution Reaction. *Adv. Mater.* **2026**, *38*, e13213. https://doi.org/10.1002/adma.202513213.
58. Shi, Z.; Liu, J.; Gao, Y.; et al. Asymmetric supercapacitors based on La-doped MoO_3 nanobelts as advanced negative electrode and VOR nanosheets as positive electrode. *J. Mater. Sci.* **2021**, *56*, 1612–1629. https://doi.org/10.1007/s10853-020-05284-0.
59. Thalji, M.R.; Al Mahmud, A.; Mahmoudi, F.; et al. Ethyl xanthate-driven in situ synthesis of Ni-Fe sulfide@$Ti_3C_2T_x$ MXene hybrid electrodes for ultra-high-performance supercapacitors. *Chem. Eng. J.* **2025**, *522*, 167789. https://doi.org/10.1016/j.cej.2025.167789.
60. Kholghi, A.; Abedi, R.; Sedighi, A.; et al. Binder-Free Direct Electrodeposition of High-Activity Sites MnO_2 Nanosheets@NiO Nanotubes as a Multifunctional Electrode for Supercapacitor Applications and Hydrogen and Oxygen Evolution Reactions. *ACS Appl. Energ. Mater.* **2026**, *9*, 4702–4721. https://doi.org/10.1021/acsaem.5c04013.
61. Zhang, X.; Zhang, F.; Wei, D.; et al. Design and synthesis of K-doped tremella-like δ-MnO_2 for high-performance supercapacitor. *J. Energy Storage* **2023**, *72*, 108468. https://doi.org/10.1016/j.est.2023.108468.
62. Zhao, Y.; Chang, C.; Teng, F.; et al. Defect-Engineered Ultrathin δ-MnO_2 Nanosheet Arrays as Bifunctional Electrodes for Efficient Overall Water Splitting. *Adv. Energy Mater.* **2017**, *7*, 1700005. https://doi.org/10.1002/aenm.201700005.
63. Gao, Z.; Zhao, Z.-h.; Wang, H.; et al. Jahn–Teller Distortions Induced by in situ Li Migration in λ-MnO_2 for Boosting Electrocatalytic Nitrogen Fixation. *Angew. Chem. Int. Ed.* **2024**, *63*, e202318967. https://doi.org/10.1002/anie.202318967.
64. Zhang, Z.; Zheng, J.; Chen, X.; et al. Achieving ultra-long cycling life for MnO_2 cathode: Modulating Mn^{3+} spin state to suppress Jahn–Teller distortion and manganese dissolution. *Energy Storage Mater.* **2025**, *76*, 104128. https://doi.org/10.1016/j.ensm.2025.104128.
65. Wang, H.; Wang, Y.; Sun, J.; et al. Needle-like nanostructured Mn_3O_4@MnO_2/C composites with boosted electrochemical performance as high-performance supercapacitor electrodes. *J. Electroanal. Chem.* **2025**, *992*, 119279. https://doi.org/10.1016/j.jelechem.2025.119279.
66. Zhang, A.; Mao, N.; Zhong, Y.; et al. Synthesis of petaloid and origami-lantern shaped MnO_2/Co_2CH@C hierarchical core-shell nanorod arrays for portable asymmetric supercapacitor. *Compos. Part B Eng.* **2021**, *215*, 108756. https://doi.org/10.1016/j.compositesb.2021.108756.
67. Zheng, X.; Liu, X.; Yang, X.; et al. Templating preparation of cannular congeries of MnO_2 and porous spheres of carbon and their applications to high performance asymmetric supercapacitor and lithium-sulfur battery. *Colloids Surf. A Physicochem. Eng. Asp.* **2021**, *610*, 125740. https://doi.org/10.1016/j.colsurfa.2020.125740.
68. Patra, P.; Laha, S.; Ghosh, S. Exfoliated Cobalt-Doped Manganese Oxide Nanosheets: An Efficient and Stable Electrocatalyst for Hydrogen Evolution Reaction in an Alkaline Medium. *ACS Appl. Energ. Mater.* **2024**, *7*, 3577–3589. https://doi.org/10.1021/acsaem.3c03022.
69. Sun, H.; Chen, S.; Zhang, B.; et al. Cation-doped sea-urchin-like MnO_2 for electrocatalytic overall water splitting. *Dalton Trans.* **2023**, *52*, 17407–17415. https://doi.org/10.1039/D3DT03059H.
70. Denisdon, S.; Senthil Kumar, P.; Boobalan, C.; et al. Hydrothermally Synthesized rGO/MnO_2/MoS_2 Nanohybrids as Superior Bifunctional Electrocatalysts for Oxygen and Hydrogen Evolution Reactions. *Langmuir* **2024**, *40*, 17753–17766. https://doi.org/10.1021/acs.langmuir.4c02192.
71. Wei, J.-X.; Cao, M.-Z.; Xiao, K.; et al. In Situ Confining Pt Clusters in Ultrathin MnO_2 Nanosheets for Highly Efficient Hydrogen Evolution Reaction. *Small Struct.* **2021**, *2*, 2100047. https://doi.org/10.1002/sstr.202100047.